Contact of the intrinsic magnetic topological insulator $Mn(Bi, Sb)_2Te_4$ with a superconducting Pb film

D. A. Estyunin,[1,*] T. P. Makarova,[1] K. A. Kokh,[1,2,3] O. E. Tereshchenko,[1,4,5] A. M. Shikin,[1] and I. I. Klimovskikh[1,6]

[1]*Saint Petersburg State University, 198504 Saint Petersburg, Russia*
[2]*V.S. Sobolev Institute of Geology and Mineralogy, 630090 Novosibirsk, Russia*
[3]*Kemerovo State University, Kemerovo, 650000, Russia*
[4]*Novosibirsk State University, 630090 Novosibirsk, Russia*
[5]*Rzhanov Institute of Semiconductor Physics, 630090 Novosibirsk, Russia*
[6]*Moscow Institute of Physics and Technology, Dolgoprudny, Moscow 141700, Russia*

(Received 29 June 2022; revised 24 September 2022; accepted 17 October 2022; published 21 October 2022)

Intrinsic magnetic topological insulators (MTIs), such as an $MnBi_2Te_4$ family, have proved to be an essential platform for the study of various quantum effects and can be used for a range of applications from information storage and dissipationless spin and charge transfer to quantum computers. The latter requires the creation of Majorana fermions, which are expected to emerge when a superconductor is contacted with an MTI surface. Therefore the study of the features arising at the interface between the MTI and the superconductor is of great interest. For this purpose in this paper, the gradual growth of the elemental superconductor (Pb) film on the surface of $Mn(Bi_{0.7}Sb_{0.3})_2Te_4$, which has a Dirac point near the Fermi level, was experimentally investigated by ARPES and XPS methods. We observed that the shape of the Dirac cone state remains almost unchanged up to coverage of ∼1.5 Pb monolayers, thus remaining topological properties of the material. It was shown that Pb atoms deposition results in surface modification. They detached upper Te atoms and form TePb alloy on the surface. Moreover, Pb deposition leads to disorder of Te, Bi(Sb) layers closest to the surface. As a result, the localization of the Dirac cone state shifts towards the bulk. All these features should be taken into account in the implementation of a topological superconducting state based on the $Pb/Mn(Bi,Sb)_2Te_4$ systems.

DOI: 10.1103/PhysRevB.106.155305

I. INTRODUCTION

Topological superconductors are a peculiar class of superconductors which is of a great interest in condensed matter physics [1]. Such materials can host Majorana bound states within the bulk superconducting gap which potentially applicable to the fault-tolerant quantum computation [2–8]. The main approach for Majorana fermions realization is to create the 2D chiral *p*-wave superconductor phase by means of conventional *s*-wave superconductor pairing to the helical Dirac surface state of topological insulator (TI) [2]. It can be achieved by the topological proximity effect [9]. This effect enables the topological surface state (TSS) to propagate into the superconductor and form a combined structure of the Dirac cone with superconducting states. Realization of this effect was shown for a thick Pb film deposited on top of topological insulator $TlBiSe_2$ [10]. To obtain Majorana fermions time reversal symmetry (TRS) in TI has to be broken and the band gap in the TSS at the Fermi level has to be opened [2–4,11].

These properties can be achieved in a magnetic TI even without external magnetic field i.e., when TI is in quantum anomalous Hall state [12,13]. At the moment, the most advanced platform for this is the intrinsic magnetic TI $MnBi_2Te_4$ (MBT) [14–22]. MBT has higher magnetic ordering temperature (∼25 K), larger theoretically predicted band gap at the Dirac point and significantly better ordering of magnetic atoms within volume in comparison to magnetic TIs doped with magnetic metals [12,13,23–27]. Indeed, it has been shown that MBT films reveal a relatively high transition temperature to the quantum anomalous Hall state [28–30].

Further, for bulk MBT crystals, the Dirac point should be shifted to the Fermi level since they are highly *n*-doped. This can be done by partial substitution of Bi atoms by Sb obtaining $Mn(Bi_{1-x}Sb_x)_2Te_4$ compound [31–35]. For bulk crystals, it was shown that the charge neutral point is at $x = 0.3$ [32]. It is worth noting that this level of substitution of Bi for Sb does not lead to a significant change in the magnetic properties [32].

The next step to obtain a system in which topological superconductivity can be realized is to form a contact between MBT with a Dirac point at the Fermi level with a superconducting material. However, the creation of contact between the two structures can result in a number of features arising at their interface. In order to analyze them, in this paper, we investigated the electronic structure of magnetic TI $Mn(Bi_{0.7}Sb_{0.3})_2Te_4$ (MBST) in contact with Pb films of different thicknesses. By means of angle-resolved photoemission spectroscopy (ARPES), it was shown that the Dirac cone (DC) state and its shape are conserved for any thickness of Pb up to ∼1.5 Pb monolayers (ML), i.e., ∼4.3 Å. However, the DC state intensity is significantly reduced. This may relate to surface modification due to its active interaction with Pb. In

*estyunin@gmail.com

order to analyze the effect of Pb atoms on the surface atoms of MBST depending on the Pb film thickness and arrangement was studied using density functional theory (DFT). It was found that Pb atoms tend to form the alloy with the upper Te atoms and detach them from the TI. In addition, the presence of Pb atoms on the surface leads to disorder of several upper MBT layers and to the shift of the TSS deeper into the sample volume. The revealed features of the interaction of Pb with MBT should be considered in the implementation of the topological proximity effect in this system.

II. RESULTS AND DISCUSSION

In the work, we deposited Pb on the MBST surface in several steps. ARPES and XPS spectra were measured at each step to control occurred changes. One deposition lasted for $4 \times N$ minutes, which should approximately correspond to $0.5 \times N$ ML of Pb according quartz microbalance control (see "Methods" section). During deposition the sample temperature was kept at ~100 K. Figures 1(a) and 2(a) show resulting XPS and ARPES spectra with different Pb coatings (labeled as deposition times in minutes: Pb4 is 4 minutes, etc.). The correspondence between time and film thickness will be presented further [Fig. 1(e)] as it is ambiguous and requires discussion.

XPS measurements. Figure 1(a) shows the XPS spectra measured at each step of Pb deposition. One can see that the intensity of the Pb 5*d* component consistently increases, while the intensity of the other components (Bi 5*d*, Sb 4*d*, and Te 4*d*) decreases. Moreover, additional components (labeled as 1 and 3) with low binding energy appear for Bi 5*d* and Sb 4*d* doublets even at the first deposition of Pb (Pb4). These components, which are satellites of the main components 2 and 4, occur as the reaction of topmost Bi and Sb atoms on the deposition of Pb. One can see that components 2 and 3 for Sb 4*d* coincide. To separate them, we assumed the same energy shift between components 1,3 and 2,4 during the spectra fitting. One can also see that Pb 5*d* has a double peak structure both for $j = 5/2$ (1, 2) and $j = 3/2$ (3, 4). Components 2 and 4 appear at the very beginning of deposition (i.e., Pb4). Further deposition leads to the appearance and constant increase in the intensity of components 1 and 3 shifted to lower binding energies. Therefore they can originated from Pb atoms from the formed thick layer, while components 2 and 4 from Pb atoms which are in contact with the surface of the MBST. The presence in the XPS spectra of Pb components, specific to both interfacelike interactions and volumelike Pb-Pb interactions, may indicate rather the islandlike type of Pb film growth on the MBST surface (Volmer-Weber type). However, locally it may be the layer-plus-island (Stranski-Krastanov) type of growth. Surprisingly, there is no pronounce changes in the Te 4*d* level. This peculiar behavior was also observed for other $Mn(Bi_{1-x}Sb_x)_2Te_4$ samples during Pb deposition. It may be thought that Pb atoms somehow interact with the underlying Bi/Sb layer without interaction with the upper Te layer. In order to solve this puzzle, structural optimizations by means of DFT calculations for different arrangements of Pb on top of MBT(MBST) will be presented below.

We also estimated the intensity of all components and plotted it as a function of Pb deposition time [Fig. 1(b)]. The

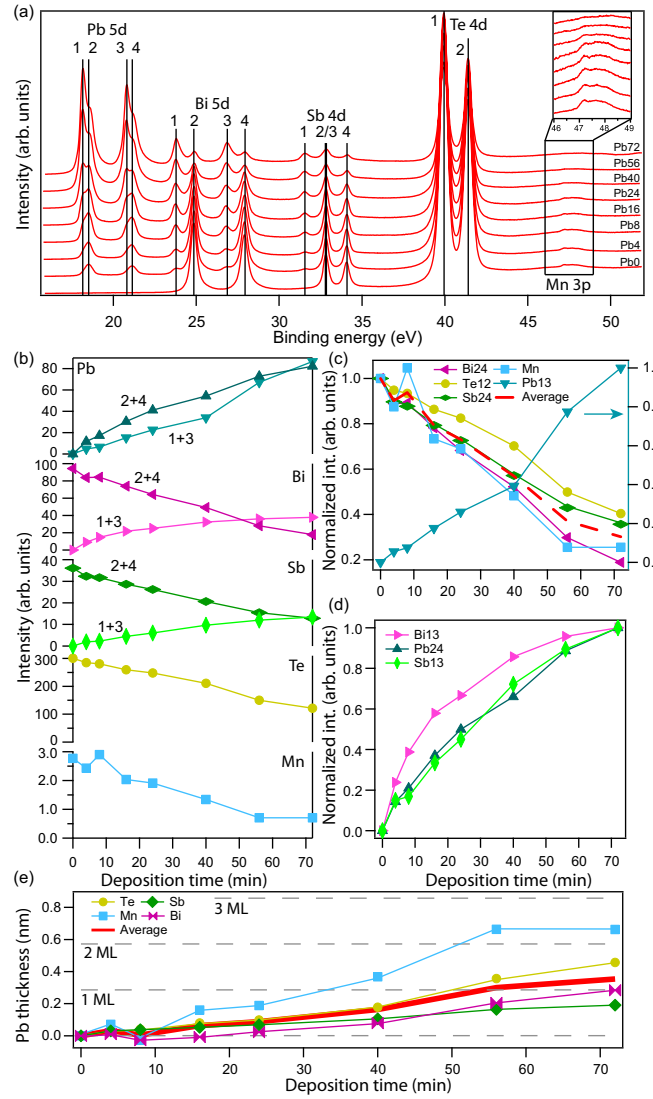

FIG. 1. (a) XPS spectra ($h\nu = 120$ eV, $T = 79$ K) for series of Pb depositions. Deposition time is shown in minutes on the right side. The numbers (1, 2, 3, 4) indicate the spectral components of each element. The inset shows a zoomed area with Mn 3*p* levels. (b) Absolute change in the intensity of elements as a function of Pb deposition time. [(c,d)] The relative change in the intensity of the components and their average value. All curves are normalized to their maximum value. The component Pb13 is referred to the right axis. (e) Correlation between the deposition time and Pb thickness determined by the intensity reduction of the different components of the spectrum. The red curve is the average of the presented curves. Horizontal lines mark the thicknesses of Pb layers.

intensity of the doublets (e.g., Bi2 and Bi4, etc.) was summed up. One can see that the behavior of Te12 and Mn coincides with the behavior of the main Bi24 and Sb24 components: their intensity decreases as the Pb film thickness increases. The behavior of the Pb13 component is opposite. For better comparison, these curves are presented together in Fig. 1(c) in a relative form. The red dashed curve shows the behavior of the averaged relative intensity of all components (Bi24, Sb24, Te12, and Mn). However, it can be seen that behavior of Bi13 and Sb13 components, arising and growing during

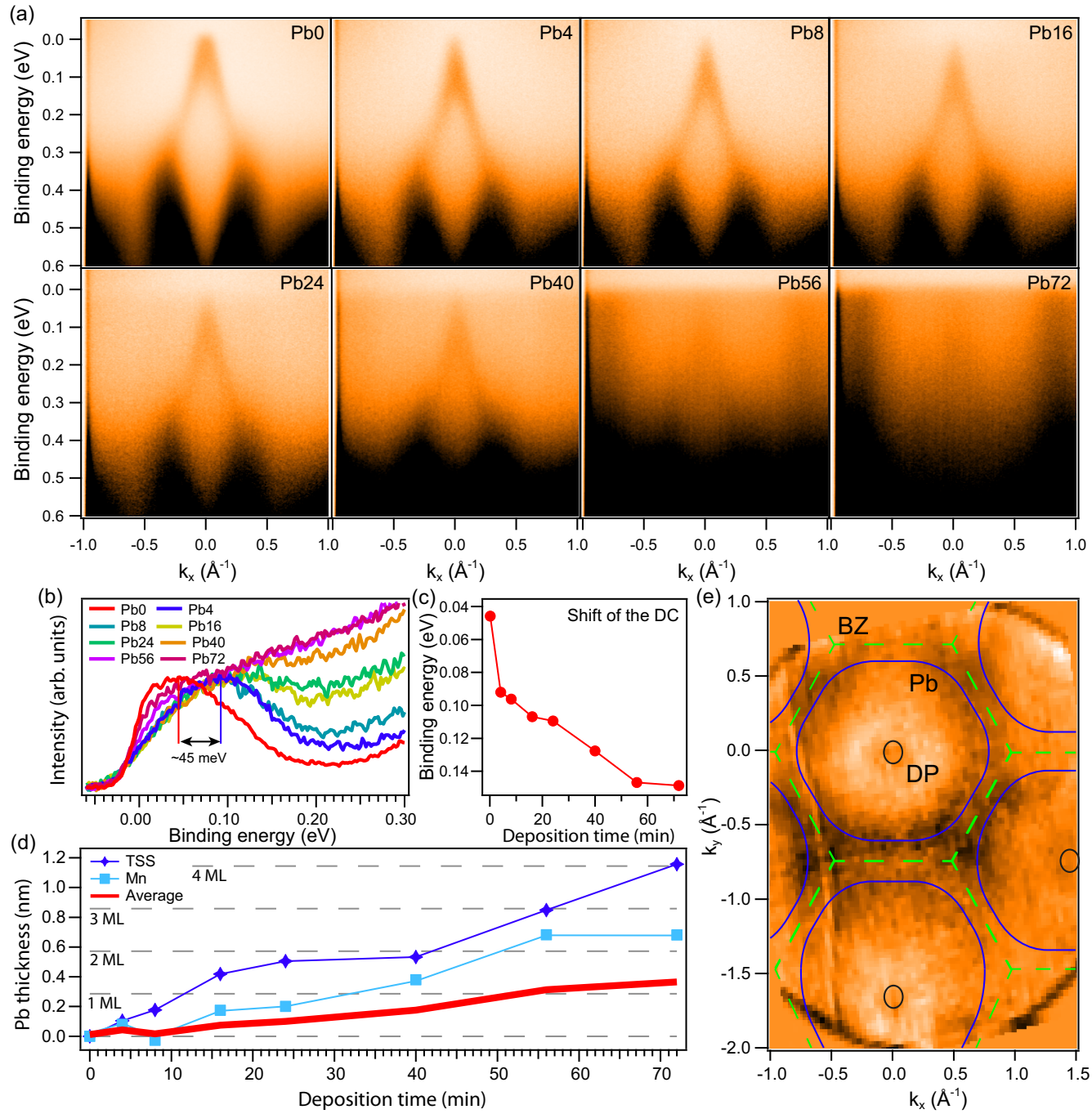

FIG. 2. (a) Dispersion relations of MBST with different amounts of deposited Pb (deposition time in minutes). Spectra were measured at $h\nu = 28$ eV and $T = 79$ K, along $\bar{\Gamma}\bar{K}$ direction. (b) EDCs at the $\bar{\Gamma}$ point, normalized to the intensity in the vicinity of the Dirac cone. (c) Dependence of the DC state shift on Pb deposition time (i.e., Pb film thickness) obtained by decomposing EDCs into spectral components. (d) Pb film thickness estimated by the DC state intensity attenuation (blue diamonds) and for comparison by Mn $3d$ (cyan squares) and by average for all peaks (red line) intensities attenuation. (e) Fermi surface of the Pb72/MBST sample measured at $h\nu = 120$ eV. Several Brillouin zones separated by green dashed lines can be seen. Pb bands (blue circles) and Dirac cone states (black circles) are marked in each zone.

Pb deposition, coincides with the behavior of the components Pb24. Thus it indicates some simultaneous process occurred for these elements. For clarity, the curves for these components are also presented together in Fig. 1(d) in a relative form.

Based on the decreasing intensity of the core levels of elements during Pb deposition, one can calculate the average thickness of the grown film. Indeed, the core level intensity (I) changes exponentially: $I = I_0 e^{-x/\lambda}$, where λ is the mean free path of an ejected electron, I_0 is the intensity of the level for the pure sample and x is the Pb film thickness. For the measurements of the XPS spectra in Fig. 1(a), photon energy of 120 eV was used. The mean free path was defined as $\lambda\,(\text{nm}) = 143/E_k^2 + 0.054\sqrt{E_k}$, where E_k (eV) is the kinetic

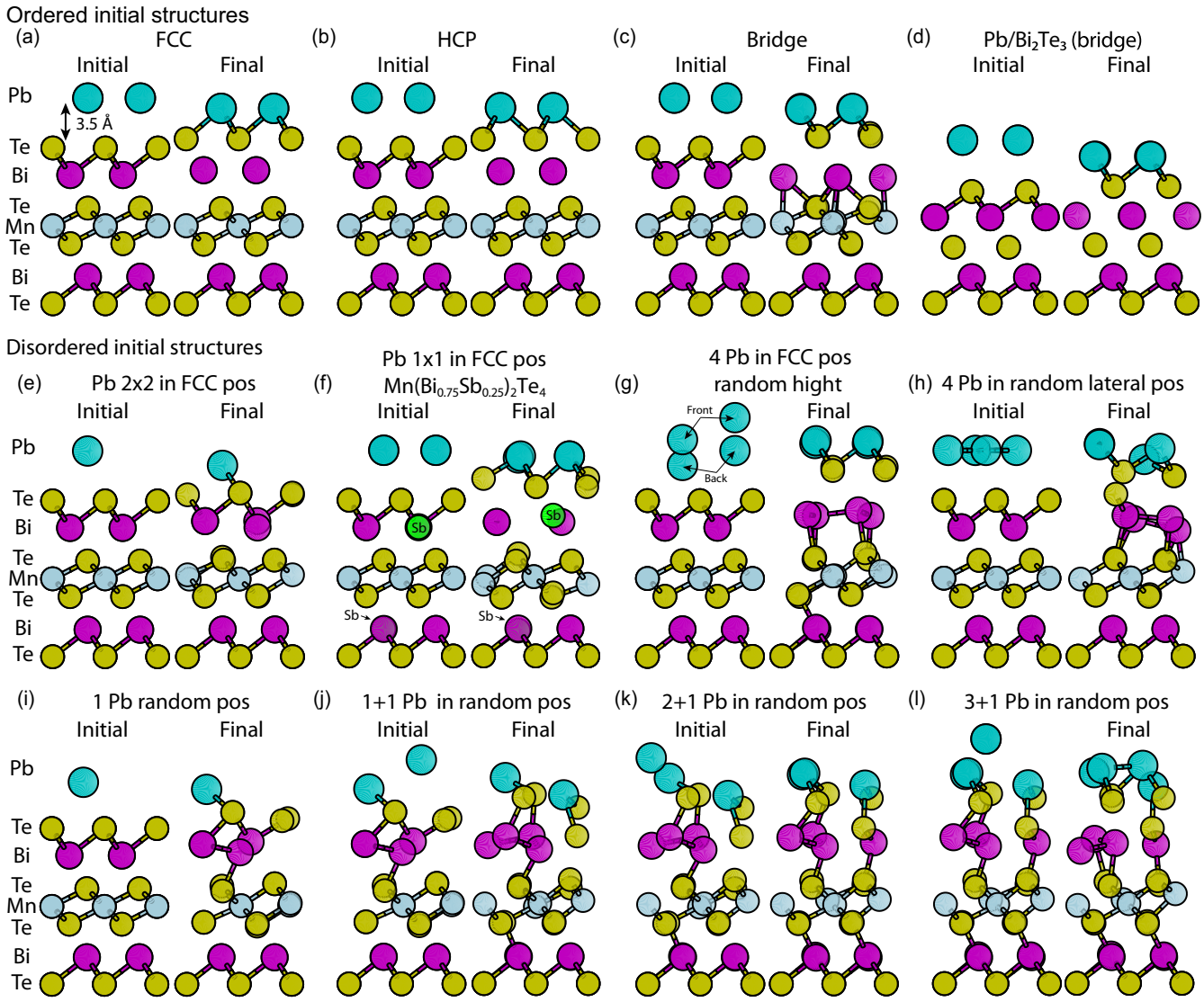

FIG. 3. A set of DFT optimized structures (initial and final) with different initial distribution/amount of Pb on the MBT(MBST) surface and Bi_2Te_3 surface in (d).

energy of the electron. For the considered levels λ slightly changes from ∼0.55 nm for Pb 5*d* to ∼0.48 nm for Mn 3*p*. Using this intensity formula, we estimated the thickness of the deposited films and established a correspondence with the deposition time [Fig. 1(e)]. However, the intensity reduction for the elements [see Fig. 1(c)] turned out to be different, resulting in various Pb thicknesses.

It is worth noting that $h\nu = 120$ eV is a rather surface-sensitive energy, so the main contribution to the intensity will be from the surface atoms and will drop significantly with increasing depth. Indeed, considering the exponential reduction of the intensity from the deep atoms, the intensity from the top Te layer will be ∼54% of the total intensity, the intensity from the subsequent Te layers in the first SL (layers 3, 5, and 7) will be ∼33%, and the intensity from the remaining bulk is only ∼13%. Thus the changes in the XPS spectra are strongly related to changes in the surroundings of the surface atoms and surface modification.

For Mn, almost 90% of the total intensity at this energy is attributed to the Mn atoms in the first SL. Moreover, Mn is located sufficiently deep from the surface to be strongly influenced by surface modification (will be shown in the section with DFT calculations, Fig. 3). Thus one would expect that the thickness of the Pb film would be well defined by the change in intensity of Mn 3*p*. The estimated thickness is shown in Fig. 1(e) (blue curve). One can see that in this case the thickness (about 2.5 ML) is larger than in the case of use of Te 4*d*, Sb 4*d*, or Bi 5*d* peaks, for which the thickness was in the range of 0.8 to 1.5 ML. This can be related both to the error in determining the intensity of the quite weak Mn 3*p* peak [see inset in Fig. 1(a)] and to the possible disordering of atoms in the near surface layers. Disorder can lead to a reduction in the diffraction component of the XPS signal, which has a stronger effect on the Mn levels, since almost all the signal comes from Mn in the first SL. Indeed, as will be shown in the DFT calculations section, Pb leads to a disorder

in the top Te and Bi(Sb) layers and stretching of the upper part of SL by about 0.6 Å.

Thus the thickness of the Pb film should be rather closer to that determined from the intensity attenuation of the Te 4*d* peak - about 1.5 ML. Also the average of all components (red solid curve) gives a final thickness of about 1.2 ML. It is worth noting that the Pb evaporator, was preliminary calibrated with a quartz microbalance, according to which the final thickness should have been about 7 ML (see Methods). Thus on the average sticking coefficient can be estimated to be about 0.2 of the quartz one, however, it can be gradually change under Pb deposition.

ARPES measurements. Figure 2(a) shows ARPES spectra measured after each step of Pb deposition. It can be seen that the DC state is conserved and visible for all Pb coatings. However, starting from Pb56 coating, it becomes weakly resolvable, while the background intensity becomes dominant. Also, intensity from additional bands appears at about $k = \pm 0.75$ Å^{-1}. We refer it to the bands from the grown Pb film. These bands are better visible at the Fermi surface plot in Fig. 2(e) and have a circular shape similar to Ref. [10]. They appear in each Brillouin zones. In addition, in Fig. 2(a), one can see the increasing intensity of the background below the Fermi level. This indicates that the system becomes metallic under Pb deposition.

From the energy distribution curves (EDCs) in Fig. 2(b) for Pb0 (red curve), one can see that there is one peak, which refers to the bottom part of the DC state. The upper part of the cone is above the Fermi level. Even this peak is slightly cut by the Fermi level, i.e., the Dirac point is above the Fermi level. The first deposition of Pb leads to a noticeable shift of the bands toward higher binding energies by about 45 meV [see the red - Pb0 and blue - Pb4 EDCs in Fig. 2(b)]. This can also be seen by comparing the ARPES spectra for these depositions: in the case of Pb4, the top of the cone becomes sharper. Figure 2(c) shows the positions of the bottom part of the Dirac cone as a function of the deposition time (thickness) of Pb. One can see that further deposition additionally shifts the Dirac cone for ∼55 meV (∼100 meV in total), reaching saturation at BE=145 meV (Pb56 and Pb72).

Pb deposition also leads to the attenuation of the DC state intensity, similar to the attenuation of core levels intensity [Fig. 1(b)]. Thus one can estimate the thickness of the deposited Pb (x) from the DC state intensity attenuation. Here it is also assumed that the intensity (I) varies according to the exponential law: $I = I_0 e^{-x/\lambda}$, where $\lambda \approx 0.47$ nm and I_0 is the DC state intensity for pure MBST. In order to estimate I, the EDCs at the $\bar{\Gamma}$ point were decomposed into spectral components, carefully excluding the metallic background. The evaluated dependence of Pb film thickness on the deposition time is shown in Fig. 2(d) (blue diamonds). Thickness estimations using the Mn 3*p* peak (cyan squares) and the average of all peaks (red curve) are also presented for comparison. One can see that the blue curve (DC state) gives a greater thickness than even the cyan curve obtained for the Mn 3*p* level. This suggests that DC state change its localization under Pb deposition and shifts deeper into the bulk compared to pure MBST (at least its localization does not shift closer to the surface). Thus, in the case of MBST (MBT), we observe the opposite situation with respect to $TlBiSe_2$ [10]: DC state tends to shift away from the grown Pb film. This can be caused by surface degradation due to the active interaction of Pb with the Te surface layer.

DFT calculations. To study the influence of Pb atoms on the crystal structure of MBT (MBST), we performed structural optimization of several Pb/MBT(MBST) structures by means of DFT. The aim was to understand the possible trends in the interaction of thin submonolayer Pb films with the MBT (MBST) surface and to explain the appearance of additional components of Bi 5*d* (Sb 4*d*) peaks and the absence of changes in Te 4*d* peaks.

A slab ($2 \times 2 \times 1$) consisting of one SL thick with twice the lateral lattice period ($a, b = 8.3$ Å) was used for structural optimization, see Fig. 3. The parameters were taken from the optimization of the MBT bulk structure. During slab optimization the bottom Te layer (closest to the van der Waals spacing) was fixed, the remaining atoms could move freely (see Methods).

Firstly, we studied initially ordered Pb films with 1×1 structure (top row of Fig. 3). Pb atoms were originally placed in FCC (above the Te atom in layer 3), HCP (above the Bi atom in layer 2) and bridge (position between FCC and HCP) positions at a distance of ∼3.5 Å from the surface. The results of the optimizations are shown in Figs. 3(a)–3(c). In all studied cases, Pb atoms and atoms of MBT remain ordered, there is no significant interlayer mixing. Also in all cases, the Pb atoms detach the surface Te atoms. This leads to the formation of the TePb alloy. Indeed, the formation energy of this compound is lower than for Bi_2Te_3. This compound has a cubic lattice ($Fm\bar{3}m$) similar to NaCl (RockSalt type). On the surface of MBT TePb is cut along the plane (111), which has hexagonal ordering of the atoms within the layer. TePb is an insulator and belongs to the trivial phase of crystalline TI $Pb_{1-x}Sn_xTe$ [36].

The strongest detachment of Te layer was observed for the bridge position. The total energy for the optimized structure is lower (i.e., the state is more favorable in terms of energy) than the energies for the optimized FCC and HCP structures (also $E_{fcc} < E_{hcp}$). In the resulting structure, the angle between Pb and Te atoms is close to 90° and the distance between them is about 3 Å (3.28 Å in bulk TePb).

Thus one can see that Pb atoms tend to detach the surface Te atom in MBT. This also affects the underlying Bi layer and can lead to its displacement. In the TePb compound, Te preserves the valence (Te^{2-}) as it has in MBT (MBST). As Te atoms are bonded to Pb atoms, the underlying Bi atoms have unpaired electrons (dangling bonds), which should lowers their binding energy.

Exactly such a situation we observe in XPS spectra of Fig. 1: the formed satellites of Bi 5*d* and Sb 4*d* peaks are related to atoms in the second layer, which appeared to have unpaired electrons. During further deposition Pb atoms cover more surface area and detach more surface Te atoms, which leads to an increase of Bi13 and Sb13 component intensities together with Pb24 component intensity [Figs. 1(b) and 1(c)]. Eventually, most of the TI surface is covered and the intensity of these components slowly reaches saturation (Pb56 and Pb72). Pb has island type of growth, so Pb13 component, which are related to bulk Pb atoms and not bonded to Te atoms, grows in parallel with Pb24 component. Indeed, during

further deposition Pb13 component accelerates its growth and becomes dominant.

We also studied how the different coatings and the initial arrangement of the Pb atoms affect the optimized structure (initially disordered structures: middle and bottom lines in Fig. 3). In general, the presence of uncompensated lateral forces leads to a disordered structure in the Pb layer and top Te and Bi layers. The underlying layers are practically unaffected and remain close to their original position. It is worth noting that the highly symmetrical position of the Pb atoms (FCC and HCP) turns out to be unstable. For example, this can be seen for structures in which Pb atoms were initially in a 2×2 structure in the symmetrical position (e) and shifted from it by $\sim$10% (i). Symmetric position of Pb is conserved after optimization of the structure, however, some of the atoms in the underlying layers leave their planes. In the case of asymmetric position there is significant atoms displacement from their initial positions. The presence of one Sb atom substituting Bi in the lattice (f) also leads to a disorder of Te, Bi(Sb), Mn atoms for the initially ordered Pb 1×1 layer in the symmetrical positions opposite to the case in Fig. 3(a). We also considered two cases in which Pb atoms were disordered in height but put in symmetrical positions (g) or Pb atoms were of the same height but in arbitrary lateral positions (h). It can be seen that in both cases Pb atoms effectively detach the surface Te layer and partially the underlying Bi layer. However, in the case of the Pb arrangement in symmetrical positions, the atomic layers appeared to be more ordered.

During deposition, Pb atoms are likely to be deposited on the surface in arbitrary positions both in height and laterally. Therefore we also carried out structural optimization in which the Pb atoms were added one by one in arbitrary positions (i)–(l). In the final optimized structure (l), the atoms formed corresponding layers, with some intermixing. Thus the general trend of Pb behavior on the MBT(MBST) surface is maintained. It is worth noting that the atoms from third layer (Te) do not have significant displacement. Consequently, the interface between Pb and MBT should be disordered. Indeed, a similar, partially disordered upper layer of Pb with islands of Pb on top of it can be attributed to the "wetting layer" found by scanning tunneling microscopy measurements for Pb/Bi_2Te_3 system [8].

It is worth noting that the optimization of Pb/Bi_2Te_3 structures shows similar results compared to the optimization of Pb/MBT structures, although with some slight differences. In the case of Bi_2Te_3 substrate [e.g., Fig. 3(d)], it can be seen that the TePb alloy is also formed, however, it appears less detached from the TI surface than in the case of MBT. It seems that the strong detachment of the TePb surface layer in MBT is a consequence of the weakened interaction between the second (Bi) and the third (Te) layers in MBT due to the embedded MnTe block. In Bi_2Te_3, the layers appear to be more strongly bonded, so the detachment of the upper layer is less beneficial than the formation of a six-layer surface block. The presence of Pb in asymmetric positions on the Bi_2Te_3 surface also leads to the layer disorder as in MBT. In general one can conclude that Pb atoms strongly interact with the surface of bismuth (antimony) telluride based TI, leading to an amorphous layer at their interface.

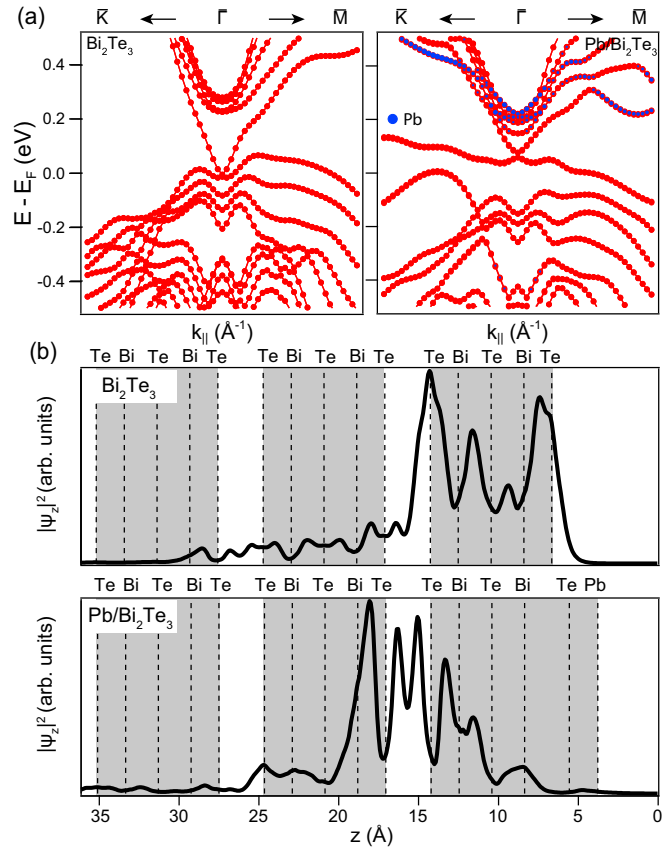

FIG. 4. (a) DFT calculated bands for Bi_2Te_3 structure and for optimized Pb/Bi_2Te_3 structure. Blue dots show projection on Pb bands. (b) Spatial distribution of TSS for Bi_2Te_3 and Pb/Bi_2Te_3. The grey rectangles indicate the quintuple layer blocks.

In the cases in (c), (g), and (h), the upper Te layer is effectively detached by Pb atoms and as a result the distance between the Te layer and the underlying Bi layer becomes about 2.8–3 Å, which is comparable to the van der Waals spacing between SLs. The TePb is also a trivial insulator. Thus one can expect that the boundary of TI shifts deeper from surface together with the density of TSS. The surface degradation that can be observed when optimising disordered structures (e)–(l) can further enhance this effect.

To test the shift of TSS localization, we used a Pb/Bi_2Te_3 structure in which the TePb layer was assumed to form on the surface at a distance of 2.8 Å from the underlying Bi layer similar to the optimized Pb/MBT structures in Fig. 3. The system Pb/Bi_2Te_3 was taken to simplify the analysis since in the case of MBT it is known that even the choice of cell parameters can affect the TSS localization and band structure [37]. Since Pb affects mainly 2 to 3 upper layers (Te-Bi-Te), we can expect that for both systems the results will be similar. The positions of the layers are shown in Fig. 4(b). Figure 4(a) shows the DFT calculations of the electronic structure of Bi_2Te_3 and Pb/Bi_2Te_3. It can be seen that for Pb/Bi_2Te_3 the Dirac cone is conserved, but its shape is slightly changed. The calculated dispersion relations are in good agreement with those previously obtainment in the experiment [38]. Additional Pb bands appear in the conduction band (projection is shown by blue circles). They do not contribute to the Dirac

cone. Figure 4(b) shows calculated TSS localization for both cases. Indeed, it can be seen that for the Pb/Bi_2Te_3 structure the TSS is significantly shifted from the surface and located at the boundary between the first and second quintuple layer blocks. It is worth noting that for the optimized Pb/Bi_2Te_3 structure in Fig. 3(d), the TSS localization also shifted away from the surface. However, Pb states are present in both the conduction and valence band and more affect the TSS cone structure.

In the case of MBT(MBST), TSS is initially quite deeply localized: the maximum is at the bottom of the first SL [39,40]. The deposition of Pb on the surface can shift TSS localization even further into volume. It was shown in Ref. [39] that the change of TSS localization can lead to a change in the band gap at the Dirac point. Thus the deposition of Pb potentially can manipulate the size of the band gap in MBT (MBST).

III. CONCLUSION

Summing up the results it can be noted that the Dirac cone is conserved under growth of Pb thin film on top of $Mn(Bi_{0.7}Sb_{0.3})_2Te_4$ surface for any deposited thickness up to ~1.5 Pb ML as shown experimentally by means of ARPES. The shape of the cone remains almost unchanged, only its shift towards higher binding energies is observed. It was also found that the localization of the DC state tends to shift away from the surface. Based on structural optimizations by DFT as well as by XPS, a tendency for the deposited Pb atoms to detach the upper Te layer with the formation of TePb alloy was shown. However, the formation of an ordered Pb (TePb) layer with a 1×1 structure is highly unstable and arbitrary deposition of Pb atoms can lead to disorder of several underlying layers in the first SL (Bi, Te and slightly Mn). The presence of any deviation of Pb atoms from the highly symmetrical position contributes to such disordering. Formation of TePb and/or surface disorder cause the shift of the TSS localization into the sample volume. All these features should be taken into account in the implementation of a topological superconducting state based on the $Pb/Mn(Bi,Sb)_2Te_4$ systems.

IV. METHODS

ARPES measurements. The ARPES dispersion relations were measured at the UARPES end-station of SOLARIS synchrotron radiation center (Krakow, Poland) using the Scienta DA30 deflector analyzer. Photon energies ranging from 8 to 140 eV are applied in the experiments. Clean surfaces of the samples were obtained by a cleavage in ultrahigh vacuum before measurements. The base pressure during the experiment was better than 5×10^{-11} mbar. Samples were measured at temperatures in the range between 10 and 79 K.

Crystal growth. High-quality single crystals of $Mn(Bi_{0.7}, Sb_{0.3})_2Te_4$ were synthesized by using a modified vertical Bridgman method in Novosibirsk State University.

Pb deposition. Pb was deposited using a lead evaporator which flux was calibrated using a quartz microbalance. The calibrated deposition rate was about 0.28 Å/min (emission current 1.5 mA, high voltage 1 kV), i.e., it takes about 10 minutes to deposit 1 ML Pb (2.86 Å) [8].

DFT calculations. Structural optimization calculations were carried out within the density functional theory using the projector augmented-wave (PAW) method [41,42] as implemented in the open-source QUANTUM ESPRESSO code [43–45]. The exchange-correlation energy in PBE version of generalized gradient approximation was exploited [46]. Structural optimization were performed in scalar relativistic mode without the spin-orbit interaction. The accuracy of the real-space numerical integration was specified by the cutoff energy of 100 Ry, the total-energy convergence criterion was 10^{-7} Ry, whereas the surface Brillouin zone of the supercell was sampled with a 5×5 mesh of k points. Convergence threshold on total energy and forces for ionic minimization were 10^{-4} Ry and 10^{-3} Ry/bohr correspondingly.

ACKNOWLEDGMENTS

The authors acknowledge support by the Saint Petersburg State University (Grant No. 90383050), Russian Science Foundation (Grant No. 18-12-00062) in the part of ARPES measurements and Grant No. 22-12-20024(p-9) in the part of crystal growth. This publication was developed under the provision of the Polish Ministry of Education and Science project: "Support for research and development with the use of research infrastructure of the National Synchrotron Radiation Centre SOLARIS" under Contract No. 1/SOL/2021/2. We acknowledge SOLARIS Centre for the access to the Beamline "UARPES," where the measurements were performed. K.A.K. was supported by the State assignment of IGM SB RAS.

D.A.E., T.P.M., and I.I.K. performed ARPES experiments. K.A.K. and O.E.T. provided samples. D.A.E. made DFT calculations, wrote the manuscript, and plotted figures with the contributions from all authors. D.A.E. and I.I.K. were responsible for all the studies and conception of the work. A.M.S supervized the work and was responsible for financial support.

[1] M. Z. Hasan and C. L. Kane, Colloquium: Topological insulators, Rev. Mod. Phys. **82**, 3045 (2010).

[2] L. Fu and C. L. Kane, Superconducting Proximity Effect and Majorana Fermions at the Surface of a Topological Insulator, Phys. Rev. Lett. **100**, 096407 (2008).

[3] J.-P. Xu, M.-X. Wang, Z. L. Liu, J.-F. Ge, X. Yang, C. Liu, Z. A. Xu, D. Guan, C. L. Gao, D. Qian, Y. Liu, Q.-H. Wang, F.-C. Zhang, Q.-K. Xue, and J.-F. Jia, Experimental Detection of a Majorana Mode in the Core of a Magnetic Vortex Inside a Topological Insulator-Superconductor $Bi_2Te_3/NbSe_2$ Heterostructure, Phys. Rev. Lett. **114**, 017001 (2015).

[4] Q. L. He, L. Pan, A. L. Stern, E. C. Burks, X. Che, G. Yin, J. Wang, B. Lian, Q. Zhou, E. S. Choi, K. Murata, X. Kou, Z. Chen, T. Nie, Q. Shao, Y. Fan, S.-C. Zhang, K. Liu, J. Xia, and K. L. Wang, Chiral Majorana fermion modes in a quantum anomalous Hall insulatorsuperconductor structure, Science **357**, 294 (2017).

[5] A. M. Black-Schaffer and A. V. Balatsky, Proximity-induced unconventional superconductivity in topological insulators, Phys. Rev. B **87**, 220506(R) (2013).

[6] J. D. Sau, R. M. Lutchyn, S. Tewari, and S. Das Sarma, Robustness of majorana fermions in proximity-induced superconductors, Phys. Rev. B **82**, 094522 (2010).

[7] C.-K. Chiu, M. J. Gilbert, and T. L. Hughes, Vortex lines in topological insulator-superconductor heterostructures, Phys. Rev. B **84**, 144507 (2011).

[8] V. S. Stolyarov, S. Pons, S. Vlaic, S. V. Remizov, D. S. Shapiro, C. Brun, S. I. Bozhko, T. Cren, T. V. Menshchikova, E. V. Chulkov, W. V. Pogosov, Y. E. Lozovik, and D. Roditchev, Superconducting long-range proximity effect through the atomically flat interface of a Bi_2Te_3 topological insulator, J. Phys. Chem. Lett. **12**, 9068 (2021).

[9] T. Shoman, A. Takayama, T. Sato, S. Souma, T. Takahashi, T. Oguchi, K. Segawa, and Y. Ando, Topological proximity effect in a topological insulator hybrid, Nat. Commun. **6**, 6547 (2015).

[10] C. X. Trang, N. Shimamura, K. Nakayama, S. Souma, K. Sugawara, I. Watanabe, K. Yamauchi, T. Oguchi, K. Segawa, T. Takahashi, Y. Ando, and T. Sato, Conversion of a conventional superconductor into a topological superconductor by topological proximity effect, Nat. Commun. **11**, 159 (2020).

[11] Y. Peng and Y. Xu, Proximity-induced majorana hinge modes in antiferromagnetic topological insulators, Phys. Rev. B **99**, 195431 (2019).

[12] C.-Z. Chang, J. Zhang, X. Feng, J. Shen, Z. Zhang, M. Guo, K. Li, Y. Ou, P. Wei, L.-L. Wang, Z.-Q. Ji, Y. Feng, S. Ji, X. Chen, J. Jia, X. Dai, Z. Fang, S.-C. Zhang, K. He, Y. Wang *et al.*, Experimental observation of the quantum anomalous Hall effect in a magnetic topological insulator, Science **340**, 167 (2013).

[13] Y. Tokura, K. Yasuda, and A. Tsukazaki, Magnetic topological insulators, Nat. Rev. Phys. **1**, 126 (2019).

[14] M. M. Otrokov, I. I. Klimovskikh, H. Bentmann, D. Estyunin, A. Zeugner, Z. S. Aliev, S. Gaß, A. U. B. Wolter, A. V. Koroleva, A. M. Shikin, M. Blanco-Rey, M. Hoffmann, I. P. Rusinov, A. Y. Vyazovskaya, S. V. Eremeev, Y. M. Koroteev, V. M. Kuznetsov, F. Freyse, J. Sánchez-Barriga, I. R. Amiraslanov *et al.*, Prediction and observation of an antiferromagnetic topological insulator, Nature (London) **576**, 416 (2019).

[15] D. Zhang, M. Shi, T. Zhu, D. Xing, H. Zhang, and J. Wang, Topological Axion States in the Magnetic Insulator $MnBi_2Te_4$ with the Quantized Magnetoelectric Effect, Phys. Rev. Lett. **122**, 206401 (2019).

[16] J. Li, Y. Li, S. Du, Z. Wang, B.-L. Gu, S.-C. Zhang, K. He, W. Duan, and Y. Xu, Intrinsic magnetic topological insulators in van der Waals layered $MnBi_2Te_4$-family materials, Sci. Adv. **5**, eaaw5685 (2019).

[17] Y. Gong, J. Guo, J. Li, K. Zhu, M. Liao, X. Liu, Q. Zhang, L. Gu, L. Tang, X. Feng, D. Zhang, W. Li, C. Song, L. Wang, P. Yu, X. Chen, Y. Wang, H. Yao, W. Duan, Y. Xu *et al.*, Experimental realization of an intrinsic magnetic topological insulator, Chin. Phys. Lett. **36**, 076801 (2019).

[18] S. H. Lee, Y. Zhu, Y. Wang, L. Miao, T. Pillsbury, H. Yi, S. Kempinger, J. Hu, C. A. Heikes, P. Quarterman, W. Ratcliff, J. A. Borchers, H. Zhang, X. Ke, D. Graf, N. Alem, C.-Z. Chang, N. Samarth, and Z. Mao, Spin scattering and noncollinear spin structure-induced intrinsic anomalous Hall effect in antiferromagnetic topological insulator $MnBi_2Te_4$, Phys. Rev. Res. **1**, 012011(R) (2019).

[19] Y.-J. Hao, P. Liu, Y. Feng, X.-M. Ma, E. F. Schwier, M. Arita, S. Kumar, C. Hu, R. Lu, M. Zeng, Y. Wang, Z. Hao, H.-Y. Sun, K. Zhang, J. Mei, N. Ni, L. Wu, K. Shimada, C. Chen, Q. Liu *et al.*, Gapless Surface Dirac Cone in Antiferromagnetic Topological Insulator $MnBi_2Te_4$, Phys. Rev. X **9**, 041038 (2019).

[20] Y. J. Chen, L. X. Xu, J. H. Li, Y. W. Li, H. Y. Wang, C. F. Zhang, H. Li, Y. Wu, A. J. Liang, C. Chen, S. W. Jung, C. Cacho, Y. H. Mao, S. Liu, M. X. Wang, Y. F. Guo, Y. Xu, Z. K. Liu, L. X. Yang, and Y. L. Chen, Topological Electronic Structure and Its Temperature Evolution in Antiferromagnetic Topological Insulator $MnBi_2Te_4$, Phys. Rev. X **9**, 041040 (2019).

[21] D. A. Estyunin, I. I. Klimovskikh, A. M. Shikin, E. F. Schwier, M. M. Otrokov, A. Kimura, S. Kumar, S. O. Filnov, Z. S. Aliev, M. B. Babanly, and E. V. Chulkov, Signatures of temperature driven antiferromagnetic transition in the electronic structure of topological insulator $MnBi_2Te_4$, APL Mater. **8**, 021105 (2020).

[22] P. Swatek, Y. Wu, L.-L. Wang, K. Lee, B. Schrunk, J. Yan, and A. Kaminski, Gapless Dirac surface states in the antiferromagnetic topological insulator $MnBi_2Te_4$, Phys. Rev. B **101**, 161109(R) (2020).

[23] I. Lee, C. K. Kim, J. Lee, S. J. L. Billinge, R. Zhong, J. A. Schneeloch, T. Liu, T. Valla, J. M. Tranquada, G. Gu, and J. C. S. Davis, Imaging Dirac-mass disorder from magnetic dopant atoms in the ferromagnetic topological insulator $Cr_x(Bi_{0.1}Sb_{0.9})_{2-x}Te_3$, Proc. Natl. Acad. Sci. **112**, 1316 (2015).

[24] J. Henk, A. Ernst, S. V. Eremeev, E. V. Chulkov, I. V. Maznichenko, and I. Mertig, Complex Spin Texture in the Pure and Mn-Doped Topological Insulator Bi_2Te_3, Phys. Rev. Lett. **108**, 206801 (2012).

[25] J. G. Checkelsky, J. Ye, Y. Onose, Y. Iwasa, and Y. Tokura, Dirac-fermion-mediated ferromagnetism in a topological insulator, Nat. Phys. **8**, 729 (2012).

[26] A. M. Shikin, A. A. Rybkina, D. A. Estyunin, D. M. Sostina, I. I. Klimovskikh, V. Y. Voroshnin, A. G. Rybkin, K. A. Kokh, O. E. Tereshchenko, L. Petaccia, G. Di Santo, A. Kimura, P. N. Skirdkov, K. A. Zvezdin, and A. K. Zvezdin, Dirac cone intensity asymmetry and surface magnetic field in V-doped and pristine topological insulators generated by synchrotron and laser radiation, Sci. Rep. **8**, 6544 (2018).

[27] S. O. Filnov, Y. A. Surnin, A. V. Koroleva, I. I. Klimovskikh, D. A. Estyunin, A. Y. Varykhalov, K. A. Bokai, K. A. Kokh, O. E. Tereshchenko, V. A. Golyashov, E. V. Shevchenko, and A. M. Shikin, Magnetic and electronic properties of gd-doped topological insulator $Bi_{1.09}Gd_{0.06}Sb_{0.85}Te_3$, J. Exp. Theor. Phys. **129**, 404 (2019).

[28] Y. Deng, Y. Yu, M. Z. Shi, Z. Guo, Z. Xu, J. Wang, X. H. Chen, and Y. Zhang, Quantum anomalous Hall effect in intrinsic magnetic topological insulator $MnBi_2Te_4$, Science **367**, 895 (2020).

[29] C. Liu, Y. Wang, H. Li, Y. Wu, Y. Li, J. Li, K. He, Y. Xu, J. Zhang, and Y. Wang, Robust axion insulator and chern insulator phases in a two-dimensional antiferromagnetic topological insulator, Nat. Mater. **19**, 522 (2020).

[30] J. Ge, Y. Liu, J. Li, H. Li, T. Luo, Y. Wu, Y. Xu, and J. Wang, High-chern-number and high-temperature quantum hall effect without landau levels, Natl. Sci. Rev. **7**, 1280 (2020).

[31] S. X. M. Riberolles, Q. Zhang, E. Gordon, N. P. Butch, L. Ke, J.-Q. Yan, and R. J. McQueeney, Evolution of magnetic

interactions in Sb-substituted $MnBi_2Te_4$, Phys. Rev. B **104**, 064401 (2021).

[32] B. Chen, F. Fei, D. Zhang, B. Zhang, W. Liu, S. Zhang, P. Wang, B. Wei, Y. Zhang, Z. Zuo, J. Guo, Q. Liu, Z. Wang, X. Wu, J. Zong, X. Xie, W. Chen, Z. Sun, S. Wang, Y. Zhang *et al.*, Intrinsic magnetic topological insulator phases in the Sb doped $MnBi_2Te_4$ bulks and thin flakes, Nat. Commun. **10**, 4469 (2019).

[33] X.-M. Ma, Y. Zhao, K. Zhang, S. Kumar, R. Lu, J. Li, Q. Yao, J. Shao, F. Hou, X. Wu, M. Zeng, Y.-J. Hao, Z. Hao, Y. Wang, X.-R. Liu, H. Shen, H. Sun, J. Mei, K. Miyamoto, T. Okuda *et al.*, Realization of a tunable surface Dirac gap in Sb-doped $MnBi_2Te_4$, Phys. Rev. B **103**, L121112 (2021).

[34] L. Zhou, Z. Tan, D. Yan, Z. Fang, Y. Shi, and H. Weng, Topological phase transition in the layered magnetic compound $MnSb_2Te_4$: Spin-orbit coupling and interlayer coupling dependence, Phys. Rev. B **102**, 085114 (2020).

[35] W. Ko, M. Kolmer, J. Yan, A. D. Pham, M. Fu, F. Lüpke, S. Okamoto, Z. Gai, P. Ganesh, and A.-P. Li, Realizing gapped surface states in the magnetic topological insulator $MnBi_{2-x}Sb_xTe_4$, Phys. Rev. B **102**, 115402 (2020).

[36] S.-Y. Xu, C. Liu, N. Alidoust, M. Neupane, D. Qian, I. Belopolski, J. D. Denlinger, Y. J. Wang, H. Lin, L. A. Wray, G. Landolt, B. Slomski, J. H. Dil, A. Marcinkova, E. Morosan, Q. Gibson, R. Sankar, F. C. Chou, R. J. Cava, A. Bansil, and M. Z. Hasan, Observation of a topological crystalline insulator phase and topological phase transition in $Pb_{1-x}Sn_xTe$, Nat. Commun. **3**, 1192 (2012).

[37] A. M. Shikin, T. P. Makarova, A. V. Eryzhenkov, D. Y. Usachov, D. A. Estyunin, D. A. Glazkova, I. I. Klimovskikh, A. G. Rybkin, and A. V. Tarasov, Factors influencing the energy gap in topological states of antiferromagnetic $MnBi_2Te_4$, arXiv:2205.07501 (2022).

[38] Y. A. Surnin, I. I. Klimovskikh, D. M. Sostina, K. A. Kokh, O. E. Tereshchenko, and A. M. Shikin, Impact of ultrathin Pb films on the topological surface and quantum-well states of Bi_2Se_3 and Sb_2Te_3 topological insulators, J. Exp. Theor. Phys. **126**, 535 (2018).

[39] A. M. Shikin, D. A. Estyunin, I. I. Klimovskikh, S. O. Filnov, E. F. Schwier, S. Kumar, K. Miyamoto, T. Okuda, A. Kimura, K. Kuroda, K. Yaji, S. Shin, Y. Takeda, Y. Saitoh, Z. S. Aliev, N. T. Mamedov, I. R. Amiraslanov, M. B. Babanly, M. M. Otrokov, S. V. Eremeev, and E. V. Chulkov, Nature of the dirac gap modulation and surface magnetic interaction in axion antiferromagnetic topological insulator $MnBi_2Te_4$, Sci. Rep. **10**, 13226 (2020).

[40] A. M. Shikin, D. A. Estyunin, N. L. Zaitsev, D. Glazkova, I. I. Klimovskikh, S. O. Filnov, A. G. Rybkin, E. F. Schwier, S. Kumar, A. Kimura, N. Mamedov, Z. Aliev, M. B. Babanly, K. Kokh, O. E. Tereshchenko, M. M. Otrokov, E. V. Chulkov, K. A. Zvezdin, and A. K. Zvezdin, Sample-dependent dirac-point gap in $mnbi_2te_4$ and its response to applied surface charge: A combined photoemission and ab initio study, Phys. Rev. B **104**, 115168 (2021).

[41] P. E. Blöchl, Projector augmented-wave method, Phys. Rev. B **50**, 17953 (1994).

[42] G. Kresse and D. Joubert, From ultrasoft pseudopotentials to the projector augmented-wave method, Phys. Rev. B **59**, 1758 (1999).

[43] P. Giannozzi, S. Baroni, N. Bonini, M. Calandra, R. Car, C. Cavazzoni, D. Ceresoli, G. L. Chiarotti, M. Cococcioni, I. Dabo, A. Dal Corso, S. de Gironcoli, S. Fabris, G. Fratesi, R. Gebauer, U. Gerstmann, C. Gougoussis, A. Kokalj, M. Lazzeri, L. Martin-Samos *et al.*, Quantum espresso: a modular and open-source software project for quantum simulations of materials, J. Phys.: Condens. Matter **21**, 395502 (2009).

[44] P. Giannozzi Jr, O. Andreussi, T. Brumme, O. Bunau, M. Buongiorno Nardelli, M. Calandra, R. Car, C. Cavazzoni, D. Ceresoli, M. Cococcioni, N. Colonna, I. Carnimeo, A. Dal Corso, S. de Gironcoli, P. Delugas, R. A. DiStasio, A. Ferretti, A. Floris, G. Fratesi, G. Fugallo *et al.*, Advanced capabilities for materials modelling with quantum espresso, J. Phys.: Condens. Matter **29**, 465901 (2017).

[45] P. Giannozzi, O. Baseggio, P. Bonfà, D. Brunato, R. Car, I. Carnimeo, C. Cavazzoni, S. de Gironcoli, P. Delugas, F. Ferrari Ruffino, A. Ferretti, N. Marzari, I. Timrov, A. Urru, and S. Baroni, Quantum espresso toward the exascale, J. Chem. Phys. **152**, 154105 (2020).

[46] J. P. Perdew, K. Burke, and M. Ernzerhof, Generalized Gradient Approximation Made Simple, Phys. Rev. Lett. **77**, 3865 (1996).